An Accurate Skull Stripping Method Based on Simplex Meshes and Histogram Analysis in Magnetic Resonance Images

Francisco J. Galdames[a,d], Fabrice Jaillet[c,d], Claudio A. Perez[a,b]

[a]*Biomedical Engineering Laboratory, Department of Electrical Engineering, Universidad de Chile, Santiago, Chile*
[b]*Advanced Mining Technology Center, Universidad de Chile, Av. Tupper 2007, Santiago, Chile*
[c]*Université de Lyon, IUT Lyon 1, Computer Science Department, F-01000, France*
[d]*Université de Lyon, CNRS, Université Lyon 1, LIRIS, SAARA team, UMR5205, F-69622, France*

Abstract

Skull stripping methods are designed to eliminate the non-brain tissue in magnetic resonance (MR) brain images. Removal of non-brain tissues is a fundamental step in enabling the processing of brain MR images. The aim of this study is to develop an automatic accurate skull stripping method based on deformable models and histogram analysis. A pre-segmentation step is used to find the optimal starting point for the deformation and is based on thresholds and morphological operators. Thresholds are computed using comparisons with an atlas, and modeling by Gaussians. The deformable model is based on a simplex mesh and its deformation is controlled by the image local gray levels and the information obtained on the gray level modeling of the pre-segmentation. Our Simplex Mesh and Histogram Analysis Skull Stripping (SMHASS) method was tested on the following international databases commonly used in scientific articles: BrainWeb, Internet Brain Segmentation Repository (IBSR), and Segmentation Validation Engine (SVE). A comparison was performed against three of the best skull stripping methods previously published: Brain Extraction Tool (BET), Brain Surface Extractor (BSE), and Hybrid Watershed Algorithm (HWA). Performance was measured using the Jaccard index (J) and Dice coefficient (κ). Our method showed the best performance and differences were statistically significant ($p < 0.05$): J=0.903 and κ=0.949 on BrainWeb; J=0.895 and κ=0.943 on IBSR; J=0.948 and κ=0.973 on SVE.

Keywords: accurate skull stripping, non-brain tissue removal, brain surface extraction, brain surface simplex mesh modeling, patient specific mesh, T1W MRI

1. Introduction

Three dimensional brain images have become increasingly popular in medical applications. These images are being used for research, diagnosis, treatment, surgical planning, and image-guided surgeries. However, several pre-processing methods are required before these images can be employed, such as image registration (Klein et al., 2010), inhomogeneity correction (Wels et al., 2011), tissue classification (de Boer et al., 2010; Wang et al., 2010), analysis of cortical structure (Thompson et al., 2001), cortical surface reconstruction (Tosun et al., 2006), cortical thickness estimation (MacDonald et al., 2000), shape quantification (Park et al., 2011) and/or identification of brain parts (Zhao et al., 2010). Many of these methods achieve a brain extraction using a skull stripping process as first step, to eliminate non-brain tissue present in the image. Therefore, it is imperative to have accurate skull stripping methods available to avoid time consuming manual corrections that are not systematic and can not be applied routinely. In addition, the reliability of these processes is essential because any error at this first step will be difficult to correct in subsequent processing steps.

Many *Skull Stripping* methods have been proposed (Kapur et al., 1996; Atkins and Mackiewich, 1998; Lemieux et al., 1999; Dale et al., 1999; Ashburner and Friston, 2000; Yoon et al., 2001; Lemieux et al., 2003; Shattuck et al., 2001). Among the first commonly used methods are the Brain Extraction Tool (BET) (Smith, 2002; Jenkinson et al., 2005), Brain Surface Extractor (BSE) (Sandor and Leahy, 1997; Shattuck et al., 2001) and the Hybrid Watershed Algorithm (HWA) (Ségonne et al., 2004). In BET, a mask is initially created using two thresholds estimated from the image histogram. Then, a spherical deformable model is initialized at the center of gravity of the mask. Finally, this deformable model is pushed to the brain surface by locally adaptive forces. The BSE performs brain segmentation using a sequence of anisotropic diffusion filters, Marr-Hildreth edge detection, and morphological processing. The HWA is a hybrid method that combines the watershed edge detection algorithm with a deformable surface model which includes shape restrictions based on a brain atlas. Another of the first commonly used methods is the 3dIntracranial (Cox, 1996; Ward, 1999). This method first models the gray levels of different tissues using Gaussian functions, and extracts upper and lower boundaries to identify brain voxels. Next, a connected component analysis is carried out slice-by-slice to identify the brain, followed by a 3D envelope process over all the slices. Finally, a neighborhood analysis is performed on each voxel to include or exclude misclassified voxels.

The above mentioned methods are commonly used for comparison. BET, BSE, ANALIZE 4.0 (Richard, 2000) and modified Region Growing (mRG) (Yoon et al., 2001) methods are compared in (Lee et al., 2003). Boesen et al. compare their Min-

neapolis Consensus Strip (McStrip) (Rehm et al., 2004) method with Statistical Parametric Mapping v2 (SPM) (Ashburner and Friston, 2000), BET, and BSE in (Boesen et al., 2004). A comparison among methods HWA, BET, BSE, and 3dIntracranial was carried out in (Fennema-Notestine et al., 2006). More recently, a comparison study among HWA, BET and BSE was performed in (Shattuck et al., 2009). Among these methods HWA has the highest sensitivity in general but the lowest specificity (Fennema-Notestine et al., 2006; Shattuck et al., 2009). HWA is prone to include unwanted subarachnoid space and non-brain tissue, particularly dura, in the segmentation. By contrast, HWA seems to be more robust to the change of parameters than other methods (Shattuck et al., 2009). There are two different indices usually used to measure the overall similarity between the Gold Standard and the proposed segmentation: the Jaccard Index (J) (Jaccard, 1912) and the Dice Coefficient (κ) (Dice, 1945).

In the literature, different databases and parameters have been used in the comparisons, and therefore results vary. In (Shattuck et al., 2009), the best performance was obtained by BET closely followed by BSE, and the method with worst performance was HWA. Nevertheless, BSE and HWA showed similar performance in (Fennema-Notestine et al., 2006), as well as BET and 3dIntracranial, but BSE and HWA demonstrated better performance. All methods show that the sagittal sinus and the posterior fossa are the areas with the most false positives.

Another example of skull stripping methods is the watershed modified algorithm proposed in (Hahn and Peitgen, 2000). The method presented in (Grau et al., 2004) is also based on a watershed transformation that uses prior information. Elastic deformations based on atlas (Sandor and Leahy, 1997), level set methods (Baillard et al., 2001; Zhuang et al., 2006), and region growing algorithms (Park and Lee, 2009) have also been employed. In (Huang et al., 2006), a hybrid method combining expectation maximization and geodesic active contours is used. A method based on an implicit deformable model which is described by radial basis functions is introduced in (Liu et al., 2009). A method that uses an intensity thresholding followed by removal of narrow connections using a Bridge Burner algorithm is presented in (Mikheev et al., 2008). A more recent example also using removal of narrow connections but employing a graph theoretic image segmentation technique is (Sadananthan et al., 2010). A method that uses watershed segmentation, Gaussian mixture model clustering and a modification of BET is employed in (Merisaari et al., 2009) to segment MRI images of premature infant brains. Techniques for combining different skull stripping algorithms to improve the segmentation have also been proposed, such as the Brain Extraction Meta Algorithm (BEMA) (Rex et al., 2004). Recently, the Multi-Atlas Propagation and Segmentation (MAPS) method was presented in (Leung et al., 2011). This method generates the brain segmentation by combining many segmentations performed by atlas registration. Another recent method which uses thresholding, length scheme, and morphological operators can be seen in (Somasundaram and Kalaiselvi, 2011). The Robust Learning-Based Brain Extraction (ROBEX) system is presented in (Iglesias et al., 2011), which is based on a Point Distribution Model (PDM) adjusted by using a voxel classification with the Random Forest Algorithm. A fast level set method which uses a speedup operator is introduced in (Hwang et al., 2011). The Simple Paradigm for Extra-Cerebral Tissue Removal (SPECTRE) that is based on a watershed principle and combines elastic registration, tissue segmentation, and morphological operators is described in (Carass et al., 2011).

Deformable models have proven to be a robust method to segment MRI images, but they are sensitive to the initialization. In addition, simplex meshes (Delingette, 1999; Matula, 2002; Böttger et al., 2007; Tejos and Irarrazaval, 2009; Gilles and Magnenat-Thalmann, 2010; Galdames et al., 2011) are a simple and efficient way to implement these models and have yielded excellent results in many applications. In this paper, we report use of a simplex mesh for brain segmentation and, to avoid the initialization sensitivity problem, implementation of a pre-segmentation. This pre-segmentation ensures an optimal starting point for the deformable model. The pre-segmentation is based on histogram analysis and morphological operators, but it differs from other methods because it performs efficient comparisons with a model to guarantee a suitable result. The mesh deformation is based on the local image gray levels, and on a modeling of the tissue gray levels performed in the pre-segmentation. Therefore, local and global information is taken into account. The mesh deformation is carried out in stages, first to ensure that all the brain tissue is included, and then to refine the segmentation and remove remaining non-brain tissue. Our Simplex Mesh and Histogram Analysis Skull Stripping (SMHASS) method obtains the best performance in the most popular online databases when compared with three of the best skull stripping methods (BET, BSE, HWA). The databases used for comparison are: BrainWeb (Cocosco et al., 1997; Aubert-Broche et al., 2006), Internet Brain Segmentation Repository (IBSR) (Center for Morphometric Analysis, 1995), and Segmentation Validation Engine (SVE) (Shattuck et al., 2009). Furthermore, the method is not based on machine learning techniques (Perez et al., 2005), hence a training database is not required.

2. Methods

Most brain quantitative MRI study methods use skull stripping as a first step to eliminate non-brain tissue. The automatic method proposed in this work uses a deformable model initialized by pre-segmentation which is based on histogram analysis and is designed to eliminate most non-brain tissue.

2.1. Pre-segmentation

The pre-segmentation allows good initialization of the deformable model which is a crucial step for the final segmentation. The pre-segmentation is based on thresholds, morphological operators, and modeling by Gaussian functions. It is fast, robust, and based on the fact that the brain is the largest connected structure inside the head (Shan et al., 2002; Dogdas et al., 2005; Kovacevic et al., 2002; Chiverton et al., 2007).

Usually, MRI images have non-isotropic voxel sizes; therefore, a re-sampling is first carried out using trilinear interpolation (Meijering, 2002) to obtain an isotropic image. To compute

the thresholds, we consider that different tissue gray levels follow Gaussian statistics, and the image histogram is considered as a probability density function of the image gray levels:

$$p(i) = \frac{n_i}{N} \quad (1)$$

where n_i is the number of voxels with gray level $i = \{0, 1, 2, \ldots, W-1\}$, and N is the number of voxels in the image, i.e., $p(i)$ is the probability for a voxel to get intensity i. Usually the number of gray levels may change depending on the image, but using a fixed number of bins W will allow standardizing our analysis. We used $W = 256$ as in (Shan et al., 2002). The pre-segmentation is performed in three main steps:

2.1.1. Background Elimination

The Otsu method (Otsu, 1979) is used, which finds the threshold, T_{Otsu}, that minimizes the within-class variance between two classes. In our case, one class is formed by the very low intensity voxels corresponding to air, bone, and part of the Cerebro-Spinal Fluid (CSF) (background); and the other class is composed of the other tissues including the Gray Matter (GM) and White Matter (WM) of the brain (foreground). The within-class variance is defined as:

$$\sigma^2_{within}(T_{Otsu}) = n_B(T_{Otsu})\sigma^2_B(T_{Otsu}) + n_F(T_{Otsu})\sigma^2_F(T_{Otsu}) \quad (2)$$

where $\sigma^2_B(T_{Otsu})$ and $n_B(T_{Otsu})$ are the variance and number of voxels in the background ($p(i) < T_{Otsu}$), respectively; and $\sigma^2_F(T_{Otsu})$ and $n_F(T_{Otsu})$ are the variance and number of voxels in the foreground ($p(i) \geq T_{Otsu}$), respectively. The original image is masked using T_{Otsu}, i.e., all voxels with gray level value less than T_{Otsu} are ignored, leading to the mask, M_1, (see Fig. 1(b)) where air, bone, and most of the CSF have been removed. The removal of very low intensity voxels (background) allows focusing the processing on the tissues of interest (foreground). Next, the brain can be identified as the largest structure inside the head.

2.1.2. Brain Identification

The brain is first separated from other tissues by applying a threshold, T_s based on an image histogram, and a brain model mask as will be explained in this section. Then, the brain tissue is selected using morphological operators and 3D connected component analysis. The threshold for separating the brain is defined as:

$$T_s = T_{Otsu} + \xi(\mu_{gm} - T_{Otsu}) \quad (3)$$

where μ_{gm} is an estimation of the mean gray level of the GM, which corresponds to the highest value in the histogram of the image masked with M_1 (Fig. 1(b)). This definition is similar to the one proposed by Shan in (Shan et al., 2002), where ξ was fixed at 0.7. We have extended this definition, leading to a more flexible threshold that can be adjusted depending on the image. ξ must be high enough to separate the brain from other tissues, while preserving the removal of brain tissue. To achieve this, the ideal T_s for each image is estimated applying thresholds computed with increasing values of ξ as follows:

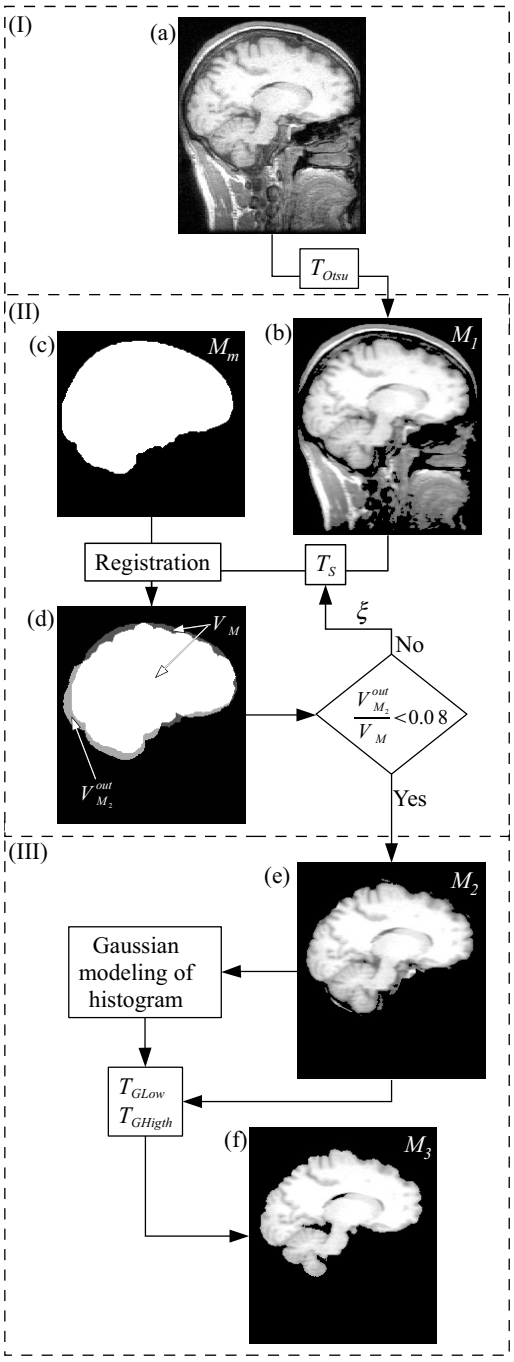

Figure 1: Flow diagram of the pre-segmentation method (which is divided into 3 steps). In step (I), an Otsu threshold T_{Otsu} is applied to the original image, (a), to eliminate background, obtaining a masked image, (b). In step (II), a threshold, T_s and morphological operators are applied to the masked image, (b), obtaining a mask, M_2 (white and light gray in (d)). The threshold, T_s is adjusted by comparing the mask, M_2 with a model mask, M_m (c) (Rex et al., 2003). To perform the comparison, M_2 and the model mask are registered. (d) Shows the registration: white represents M_m and M_2; dark gray represents only M_m; and light gray represents only M_2. Then, if the volume, $V^{out}_{M_2}$ (light gray in (d)) of M_2 that lies outside the model mask is lower than 8% of the model mask volume, V_M (dark gray and white in (d)), the image masked with M_2 (e) is used in the next step (III). Otherwise, T_s is modified to eliminate more non-brain tissue. In step (III), the gray levels of different tissues are modeled using Gaussian functions. This modeling is used to compute two thresholds, T_{GLow} and T_{GHigth}, which are used, together with morphological operators, in the image, (e). The result of this final step is a pre-segmented image, (f).

Given a value of ξ, the threshold T_s is computed using (3). Then, T_s is applied to the image masked with M_1 (Fig. 1(b)), and the resulting image is binarized. In this binarized image, small connections between brain and surrounding tissue may still remain. To eliminate them, a binary opening is applied 2 times to the mask, using a 3D spherical structural element with a 3 mm radius. Next, the mask, M_2 (Fig. 1(d)), is obtained by performing a 3D connected component analysis using a square connectivity equal to one, and keeping the largest element. The mask should have brain shape and therefore, to evaluate whether enough tissue has been removed, the resulting volume element is compared with the brain model mask which is a binary mask of the ICBM452 5th-order warp atlas from the Laboratory of Neuro Imaging at UCLA (Rex et al., 2003) (Fig. 1(c)). The model mask is registered to the mask, M_2 before the comparison. Assuming the model mask and M_2 have the same orientation, a simple and direct transformation with 6 parameters is used for the registration; 3 translations and 3 scaling operations. In the coordinate axis, the transformation matches the limits of the upper part of the brain. Because usually there are tissue remnants that can cause errors when simply the "bounding box" (limits of the whole volume in the three coordinate axis) of M_2 is used, a careful selection of the limits is performed as follows:

The rules to find the connected volume representing the brain are designed to ensure that the head will always be recognized; hence the upper reference limit is the top of the mask in the axial direction (sagittal and coronal cuts in Figure 2(a)(b)). The lower reference limit is defined as the axial position, L_{bottom}, of the bottom of the frontal lobe (sagittal cuts in Figure 2(a)(b)). To identify this landmark, a set of sagittal slices in the center of the skull is analyzed, because remaining tissue may be in the lateral parts of the head (e.g., the eyes). The center of the mask bounding box is considered to be the center of the skull; and the slices at a distance from the center less than 1/30 of the bounding box's lateral length are selected (Fig. 2(a)(b)). The bottom of the frontal lobe is identified in a profile constructed by projecting the selected slices laterally (Fig.2(c)). The profile is inspected in a caudal direction starting from the top of the head. At each step, the maximum value found on the profile, v_{max}, is updated and compared with the current value, v_c. We estimate that the axial position L_{bottom} of the bottom of the frontal lobe is the first axial slice where the current profile value, v_c, has a significant difference from the current maximum value, v_{max}. An appropriate difference is 20% of the skull length in the posterior-anterior direction. To estimate the length of the skull, v_{max} is taken as the anterior limit, and BBy_{min}, the posterior bound of the mask bounding box, is taken as the posterior limit. Therefore, L_{bottom} (Fig. 2(c)) is reached in the first slice where:

$$v_c < v_{max} - (v_{max} - BBy_{min})0.2 \qquad (4)$$

The anterior reference limit for the registration is v_{max}. The posterior reference limit is the posterior limit, B_{post}, of the projection of the central slices at the slice where v_{max} was found (Fig. 2(c)). The lateral reference limits are the bounding box lateral limits of the upper part of the mask, from the top of the head to the bottom of the frontal lobe, L_{bottom} (axial cuts in Figure 2(a) and (b)).

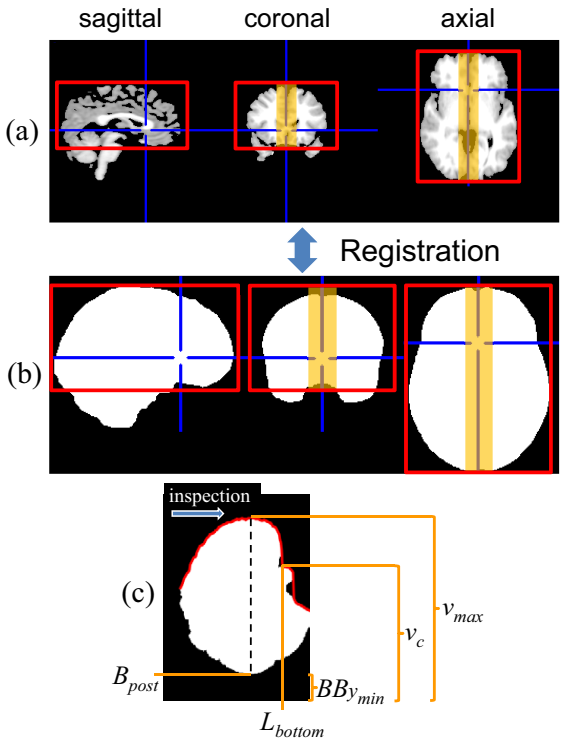

Figure 2: References used to register (a) the Pre-segmentation Mask M_2, and (b) the Model Mask. This registration is used to estimate the value of ξ in the computation of threshold, T_s. The limits used to compute the registration are marked in red. The bottom of the frontal lobe, L_{bottom}, is used as the caudal limit, which is found using the central sagittal slices marked in coronal and axial cuts (a)(b). A frontal profile (c) of the lateral projection of the central slices is used to identify the bottom of the frontal lobe, the first axial slice where $v_c < v_{max} - (v_{max} - BBy_{min})0.2$

After registration, M_2 is compared to the model mask (see Fig. 1(d)) to check whether the non-brain tissue has been properly removed. If the volume (number of voxels) of M_2 lying outside the model mask, $V^{out}_{M_2}$ (light gray in Figure 1(d)), is small enough compared to the volume of the model mask, V_M (dark gray and white in Figure 1(d)), it is assumed that the tissue removal is successful. Therefore, an empirical threshold of 0.08 is used, and the following condition should be satisfied to accept the tissue removal:

$$\frac{V^{out}_{M_2}}{V_M} < 0.08 \qquad (5)$$

Expression (5) is assessed using masks obtained with increasing values of ξ in the set $\xi = \{0.1, 0.2, \ldots, 0.9\}$. If (5) is satisfied, no more values of ξ are tested and the current mask M_2 is used in the next step of the pre-segmentation (Fig. 1(e)).

After the procedure described above, some parts of other tissues, such as dura, still remain around the brain. Thus, other thresholds are required, and they are computed by assuming that those tissues belong to a class depending on their gray levels. The classes are modeled by Gaussian functions, and the resulting model is used to compute the new thresholds (sec. 2.1.3) and as part of the information to guide the deformable model (sec. 2.2).

2.1.3. Histogram Modeling by Gaussians

Elimination of non-brain tissue is performed in this stage by the application of thresholds computed using a Gaussian approximation of the image histogram. The brain tissue is also selected using morphological operators and 3D connected component analysis (Fig. 1(III)). Based on gray level analysis, it can be assumed that image tissues belong to four classes that follow normal distribution (Shan et al., 2002; Kovacevic et al., 2002; Chiverton et al., 2007) (Fig. 3):

- C_1: Background noise, cerebrospinal fluid and dura. It may form a peak in the histogram, but often does not.
- C_2: Gray matter. It forms the central peak in the histogram.
- C_3: White matter. It forms the peak at the right side of the histogram.
- C_4: Other tissues with high gray value. Consist of very few voxels and never forms a peak.

An approximated histogram is constructed modeling these classes with Gaussians. Because class C_4 has very few voxels, only classes C_1, C_2, and C_3 are modeled. Therefore, the approximated histogram is:

$$p'(i;v) = \sum_{k=1}^{3} p_k \exp\left(-\frac{1}{2}\left[\frac{i-\mu_k}{\sigma_k}\right]^2\right) \tag{6}$$

where i is a gray level, μ_k is the mean gray level of class $k = \{1, 2, 3\}$, p_k is the probability for a voxel of class k to obtain intensity μ_k, σ_k is the standard deviation of the Gaussian function that represents the class k, $v = (\mu_k, \sigma_k, p_k)$ is the vector of parameters of the Gaussian functions, and $p'(i;v)$ is the probability that a voxel has intensity, i, using the vector of parameters, v. Thus, the values, μ_k, should correspond to the main peaks in the image histogram. The parameters of the Gaussian functions are adjusted such that $p'(\cdot;v)$ fits the image histogram. Therefore, the vector of optimal parameters $v^* = (\mu_k^*, \sigma_k^*, p_k^*)$ is:

$$v^* = \underset{v}{\operatorname{argmin}} \sum_{i=0}^{W-1} \left[p(i)) - p'(i;v)\right]^2 \tag{7}$$

where W is the number of gray levels or bins in the histogram. This minimization is performed using the Levenberg-Marquardt algorithm (Moré, 1977), which is especially suitable for minimizing functions that can be expressed as a sum of squared residuals. The initial vector of parameters for the minimization is computed using a non-parametric smoothing method. This method is based on *kernel density estimation* (Rosenblatt, 1956) which is a technique used to estimate the probability density function of a random variable. In our case, this variable is the image histogram, $p(i)$. Thus, the kernel density estimation is:

$$\hat{p}(i;h) = \frac{1}{Nh} \sum_{j=0}^{W-1} p(j) K\left(\frac{i-j}{h}\right) \tag{8}$$

where h is the bandwidth parameter, and K the kernel function. The commonly used normal distribution with mean 0 and variance 1 is used as the kernel function:

$$K\left(\frac{i-j}{h}\right) = \frac{1}{\sqrt{2\pi}} e^{-\frac{(i-j)^2}{2h^2}} \tag{9}$$

In this way, the variance is controlled indirectly through parameter h. This parameter controls the amount of smoothing of $\hat{p}(i;h)$, i.e., when h is high, $\hat{p}(i;h)$ will be smoother. Since the image histogram is seen as a probability density function, the peaks of each class correspond to main function modes. In order to localize the modes of the function, the parameter, h, is adjusted to obtain a smooth function whose number of peaks is equal to the number of modes we want to identify. The larger the value of h, the smoother the estimation $\hat{p}(i;h)$ and the fewer the number of local maxima. The adjustment of h to obtain a desired number of local maxima, m, is explained as follows.

First, two limit values for h are fixed: h_{high} and h_{low}. Since m modes should be found, h_{high} must be high enough to obtain $\hat{m} < m$ modes when it is used in the estimation, and h_{low} must be low enough to obtain $\hat{m} > m$ modes. Then, h is adjusted iteratively, providing a value, h_t at each iteration, t, starting with $h_0 = (h_{high} + h_{low})/2$:

1. Compute $\hat{p}(\cdot;h_t)$ (Eq. (8))
2. Compute the number of modes $\hat{m}$ in $\hat{p}(\cdot;h_t)$
3. **if** $\hat{m} \leq m$ **then**
   $h_{high} = h_t$
   else
   $h_{low} = h_t$
   end if
4. Compute $h_{t+1} = \frac{h_{high}+h_{low}}{2}$.
5. **if** $\hat{m} = m$ and $|h_t - h_{t+1}| < 0.001$ **then**
   return $\hat{p}(\cdot;h_{t+1})$
   else
   go to step 1.
   end if

The class C_1 does not always show a peak. Therefore, to compute the initial vector of parameters to adjust $p'(i;v)$, the best method is to find the peaks of classes C_2 and C_3. Because μ_2 and μ_3 are the highest peaks in the histogram, they can be located using the algorithm described above. Using these estimations of the mean gray levels, the initial vector of parameters $v = (\mu_k, \sigma_k, p_k)$ for the adjustment of the Gaussian functions (Eq. (7)) is obtained: $v = [\mu_2\ 0.75, \mu_2, \mu_3, W/6, W/6, W/6, \hat{p}(\mu_2\ 0.75), \hat{p}(\mu_2), \hat{p}(\mu_3)]$. This initial vector is used in the Levenberg-Marquardt algorithm to perform the minimization of equation (7), and obtain the optimal vector of parameters v^* for the approximated histogram, $p'(\cdot, v)$ (Eq. (6)). Figure 3 shows the image histogram, $p(i)$ (black dashed line), and the approximated histogram, $p'(i;v^*)$ (red line) formed by the sum of the Gaussian functions representing the gray level distributions of classes C_1 (green line), C_2 (yellow line), and C_3 (blue line). Because class C_2 represents the gray matter and class C_3 the white matter, it can be assumed that the mean value and standard deviation of the GM and WM

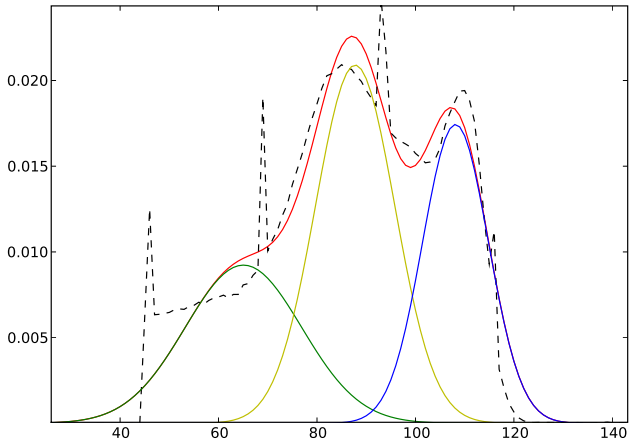

Figure 3: Histogram as a probability density function and approximated by Gaussian functions. The black dashed line represents the real image histogram, $p(i)$, and the red line is the approximated histogram, $p'(i, v)$. The approximated histogram is the sum of the estimated normal distributions of the gray levels of classes C_1 (green line, left), C_2 (yellow line, center) and C_3 (blue line, right) (sec. 2.1.3).

gray level are, $\mu_{gm} = \mu_2$, $\sigma_{gm} = \sigma_2$; and $\mu_{wm} = \mu_3$, $\sigma_{wm} = \sigma_3$, respectively.

Two final thresholds, T_{GLow} and T_{GHigh}, are computed using the estimated gray level distribution of the tissues (Shan et al., 2002):

$$\begin{aligned} T_{GLow} &= \mu_{gm} - 2.5\sigma_{gm} \\ T_{GHigh} &= \mu_{wm} + 2.5\sigma_{wm} \end{aligned} \tag{10}$$

A new mask is computed using these thresholds (Fig. 1(f)). The mask is composed of all voxels, in the image masked with M_2, having a gray level, i, that satisfies: $T_{GLow} \leq i \leq T_{GHigh}$. With the purpose of disconnecting the remaining tissues with gray levels similar to the brain, a binary opening is used in the mask. The opening operator is applied once, using a 3D spherical structural element with a radius of 4 mm. Then, to identify the brain, a 3D connected component analysis is performed in the mask, using a square connectivity equal to one. The largest element is kept, and it forms the mask, M_3. The original image masked by M_3 is the final pre-segmentation of the brain. Fig. 4 shows two orthogonal slices of the MRI pre-segmentation, in which tissues have been eliminated, except for the cerebral parenchyma (Fig. 4(c)).

2.2. Segmentation by Deformable Models

The final segmentation is carried out by deformable models, using the original and the pre-segmented images. The deformable model is based on a simplex mesh. A detailed description of simplex meshes is given by Delingette in (Delingette, 1999), where it is reported that simplex mesh properties make them suitable for a wide range of segmentation tasks. In our segmentation, a generic mesh, $\mathcal{M}$, is deformed to reach the GM-CSF interface. First, this generic mesh is geometrically adjusted using an affine transformation computed by identification of landmarks in the pre-segmented image. Next, the mesh is deformed using the pre-segmented image, and then by using the original image. The deformation of the model is carried out following three steps.

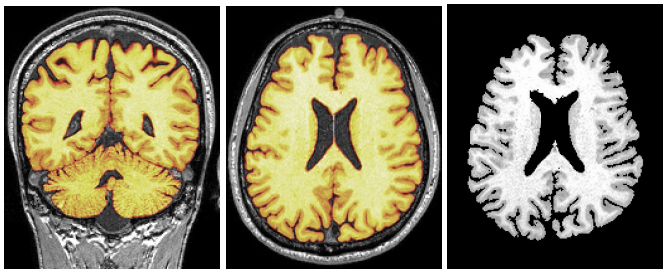

(a) (b) (c)

Figure 4: (a) Coronal and (b) Axial slice of the MRI. (c) Extraction of the cerebral parenchyma by the pre-segmentation method.

2.2.1. Initial Mesh Generation

The ICBM452 5th-order warp atlas (Rex et al., 2003) (Laboratory of Neuro Imaging (LONI) at UCLA) was used to build the generic mesh, $\mathcal{M}$. This atlas represents an average of the intensities and anatomical shapes of T1-weighted MRI images of normal young adult brains. A mesh with genus 0 was built using the well known marching cubes algorithm (Lorensen and Cline, 1987) on the ICBM452 atlas. The result of the marching cubes algorithm is a triangulation; however, a triangulation can be transformed into a simplex mesh by applying a dual operation (Galdames and Jaillet, 2010) (see Fig. 6(c)). The generic mesh does not include the *sulci* or *gyri* in details; but these structures are incorporated during the mesh deformation. The geometric adjustment of the generic mesh to the pre-segmentation volume is explained in the next section.

2.2.2. Mesh Geometric Adjustment

After pre-segmentation, a global matching of the generic mesh, $\mathcal{M}$, is carried out using geometric transformations. First, $\mathcal{M}$ is scaled and translated to match the pre-segmented MRI. The references used to carry out this transformation are found in the same way as the estimation of threshold T_s that is described in section 2.1.2. The caudal limit of the frontal lobe and the bounding box of the upper part of the brain in $\mathcal{M}$ are matched with the same references in the pre-segmented image.

Next, an affine transformation is carried out minimizing the sum of the square distances among the mesh vertices and the pre-segmented MRI edges. The optimal transformation parameters are found using the Levenberg- Marquardt minimization method. The distances in the pre-segmented MRI image are pre-computed using the distance transformation on the edges of the MRI segmentation after binarization. Figure 5(a) shows the cortex mesh after the affine transformation.

2.2.3. Simplex Meshes Applied to Brain Segmentation

In this section, simplex meshes are introduced, and the theory for their deformation is explained in relation to brain segmentation. The model is deformed using information from both pre-segmented and original images to discriminate between GM

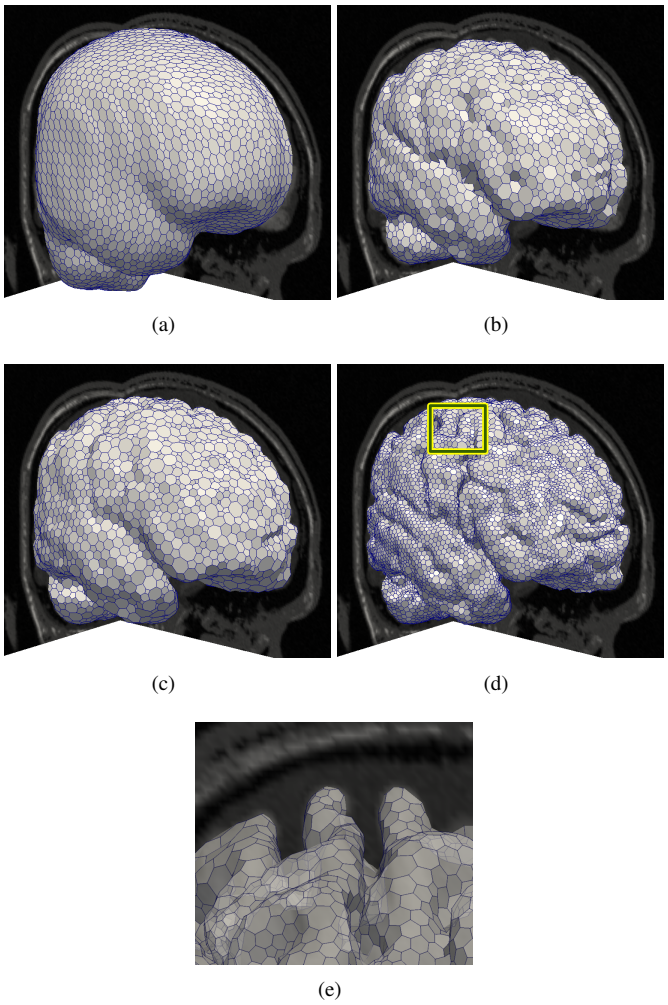

Figure 5: Examples of deformation steps with the simplex mesh: (a) After geometric adjustment by affine transformations (sec. 2.2.2). (b) After a first deformation to match the pre-segmentation (sec. 2.2.3.2). (c) After a coarse second deformation to roughly match the cortex surface. (sec. 2.2.3.3). (d) After a refined third deformation to match the sulci and gyri (sec. 2.2.3.4). (e) Zoom image of the final deformation that shows the mesh following the sulci and gyri.

and CSF in order to find the interface between them. The deformation is directed by local forces computed over the gray levels of the image.

2.2.3.1. Simplex Meshes.

A general description of simplex meshes is presented here. A k-simplex is the convex hull of k+1 independent points, e.g., a segment is a 1-simplex, a triangle is a 2-simplex, and a tetrahedron is a 3-simplex. By definition, a k-simplex mesh has a (k+1)-simplex in each vertex. For example, a 1-simplex mesh is a contour in which each vertex and its two neighbors define a triangle. This property defines the connectivity of the mesh where the vertices of a k-simplex mesh have k+1 neighbors. The types of objects that can be represented by these meshes depends on the mesh connectivity, e.g., a k-simplex mesh with k=1 can represent a curve, k=2 a surface, and k=3 a volume. To segment the brain surface, we use 2-simplex meshes. Each vertex of these meshes has three neighbors, and these four points define a tetrahedron (Fig. 6(a): $P_i, P_{N1(i)}, P_{N2(i)}, P_{N3(i)}$). An interesting feature of 2-simplex meshes is that they are the topological dual of the triangulations (meshes of triangles); making it possible to obtain a 2-simplex mesh by applying a dual operation to a triangulation, and vice versa (Fig. 6(c)). This property is useful because it is more convenient to represent a surface with a triangulation for some tasks, e.g., rendering, computing intersections, or constructing volumetric meshes. Hereafter, we will refer to 2-simplex meshes simply as simplex meshes.

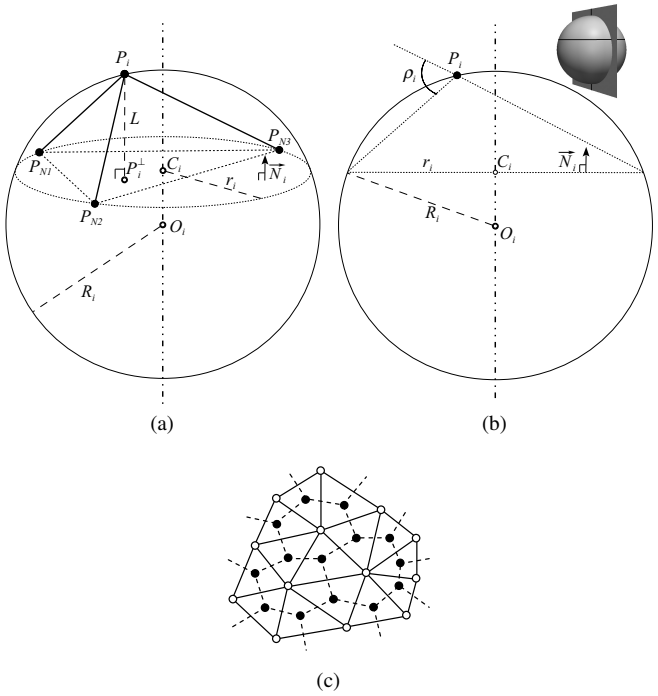

Figure 6: (a) Local geometry of a 2-simplex mesh. The tetrahedron formed by a vertex, P_i and its 3 neighbors, $P_{N1(i)}, P_{N2(i)}, P_{N3(i)}$, is shown. These four points (vertex P_i and its neighbors) define the circumscribed sphere of the tetrahedron, with center O_i and radius R_i. Also, the three neighbors define the circle with center C_i and radius r_i. (b) Simplex angle, ρ_i shown in a cut passing through the vertex P_i and the axis of the sphere $\overrightarrow{O_iC_i}$. (c) 2-simplex mesh (dark dots) and its dual triangulation (white dots).

As mentioned, each vertex of a simplex mesh positioned at P_i has three neighbors, positioned at $P_{N1(i)}, P_{N2(i)}, P_{N3(i)}$. The vertex and its neighbors form a tetrahedron (see Fig. 6(a)). It is possible to compute the tetrahedron's circumscribed sphere with center, O_i, and radius, R_i, defined by these four points, and the circle with center C_i and radius r_i defined by the three neighbors. The three neighbors also define a plane with normal $\vec{N}_i$, which includes the circle with center C_i. With these geometric entities, the simplex angle ρ_i can be defined. (See Fig. 6(b)):

$$\rho_i \in [-\pi, \pi]$$
$$\sin(\rho_i) = \frac{r_i}{R_i}\,\mathrm{sgn}\left(\overrightarrow{P_iP_{N1(i)}} \cdot \vec{N}_i\right)$$
or
$$\cos(\rho_i) = \frac{\|O_iC_i\|}{R_i}\,\mathrm{sgn}\left(\overrightarrow{O_iC_i} \cdot \vec{N}_i\right) \qquad (11)$$

where *sgn* is the *sign* function and $(\cdot)$ is the inner product. Therefore, the simplex angle ρ_i is defined in every vertex P_i by means of its neighbors $P_{N1(i)}, P_{N2(i)}, P_{N3(i)}$, and it does not depend on the position of the neighbors within the circle they define. The simplex angle and the height L (Fig. 6(a)) of P_i over the plane defined by its neighbors are related by:

$$L(r_i, d_i, \rho_i) = \frac{(r_i^2 - d_i^2)\tan(\rho_i)}{\chi\sqrt{r_i^2 + (r_i^2 - d_i^2)\tan^2(\rho_i)} + r_i}$$
$$\chi = \begin{cases} 1 & \text{if } |\rho_i| < \pi/2 \\ -1 & \text{if } |\rho_i| > \pi/2 \end{cases} \quad (12)$$

where $d_i = \left\|C_i P_i^{\perp}\right\|$, and $P_i^{\perp}$ is the projection of P_i over the plane defined by its neighbors. Since the simplex angle is scale-invariant, it can be seen as a local and scale-invariant measure of the height, L, of P_i over the plane defined by its neighbors. Moreover, the simplex angle is related to the surface curvature at P_i. It is possible to approximate the curvature at P_i by the curvature of the sphere that best fits the surface in a neighborhood around P_i. If the neighbors $P_{N1(i)}, P_{N2(i)}, P_{N3(i)}$ of P_i are considered, this sphere is the circumscribed sphere of the tetrahedron formed by the four points (Fig. 6(a)), and its mean curvature is $H_i = 1/R_i$. This mean curvature at point P_i can be expressed in terms of the simplex angle (Delingette, 1999) using (11): $H_i = \frac{\sin(\rho_i)}{r_i}$. Other important geometric entities of the simplex meshes are the metric parameters $\varepsilon_{1i}, \varepsilon_{2i}, \varepsilon_{3i}$. These parameters are the barycentric coordinates of the projection, $P_i^{\perp}$ of the vertex, P_i on the triangle defined by its neighbors (Fig. 6(a)):

$$P_i^{\perp} = \varepsilon_{1i} P_{N1(i)} + \varepsilon_{2i} P_{N2(i)} + \varepsilon_{3i} P_{N3(i)}$$
$$\varepsilon_{1i} + \varepsilon_{2i} + \varepsilon_{3i} = 1 \quad (13)$$

The position of a vertex projection on the plane defined by its neighbors is defined by (13), and the height of the vertex over this plane by (12). Therefore, the metric parameters and the simplex angle completely determine the position of the vertex as follows:

$$P_i = \varepsilon_{1i} P_{N1(i)} + \varepsilon_{2i} P_{N2(i)} + \varepsilon_{3i} P_{N3(i)} + L(r_i, d_i, \rho_i)\overrightarrow{N_i} \quad (14)$$

The simplex mesh deformation can be controlled by internal and external forces. The external forces are computed from the image, and push the mesh to the desired borders. The internal forces are computed from the mesh, considering for a smooth deformation and keeping the mesh regularity.

Now, we describe how the mesh can be deformed. The dynamics of the model are controlled by means of a Newtonian law of motion:

$$m\frac{\partial^2 P_i}{\partial t^2} = -\gamma\frac{\partial P_i}{\partial t} + \overrightarrow{F_{int_i}} + \overrightarrow{F_{ext_i}}, \quad (15)$$

where m is the mass unit of a vertex (usually 1 (Delingette, 1999)), γ is a damping factor, P_i is the position of vertex i, F_{int_i} represents the internal force at vertex i, and F_{ext_i} represents the external force. Considering discrete time and using finite differences we obtain:

$$P_i^{t+1} = P_i^t + (1-\gamma)\left(P_i^t - P_i^{t-1}\right) + \overrightarrow{F_{int_i}} + \overrightarrow{F_{ext_i}} \quad (16)$$

The internal force of a simplex mesh can be locally determined by the simplex angle, ρ_i and the metric parameters $\varepsilon_{1i}, \varepsilon_{2i}, \varepsilon_{3i}$. The internal force is derived from the minimization of a local energy, $S_i = \frac{\lambda}{2}\overrightarrow{P_i P_i^*}^2$, where P_i^* is a target position in which the vertex, i, would have simplex angle ρ_i^* and metric parameters $\varepsilon_{1i}^*, \varepsilon_{2i}^*, \varepsilon_{3i}^*$. In this way, the mesh local curvature can be controlled by the simplex angle, and the vertex position relative to its neighbors by the metric parameters. By minimizing the energy, the internal force is: $\overrightarrow{F_{int_i}} = \frac{\partial S_i}{\partial P_i} = \lambda\overrightarrow{P_i P_i^*}$. If we use (14) to express the vertex position, the internal force can be written as:

$$\overrightarrow{F_{int_i}} = \lambda\Big(\varepsilon_{1i}^*\overrightarrow{P_i P_{N1(i)}} + \varepsilon_{2i}^*\overrightarrow{P_i P_{N2(i)}} + \varepsilon_{3i}^*\overrightarrow{P_i P_{N3(i)}} + L(r_i, d_i, \rho_i^*)\overrightarrow{N_i}\Big) \quad (17)$$

In our work, the metric parameters are fixed to $1/3$, to obtain a regular mesh. The target simplex angle, ρ_i^* can be fixed in a value or computed at each iteration in a neighborhood around the vertex to obtain a curvature continuity constraint (Delingette, 1999). We perform different mesh deformations, and in each one, a different definition of the external force $\overrightarrow{F_{ext_i}}$ and ρ_i^* is used. In each deformation, (16) is iterated until the mean displacement of the mesh vertices is less than 0.01. These deformations are explained in the following sections.

2.2.3.2. First Mesh Deformation.

After the geometric adjustment (sec. 2.2.2), the mesh, $\mathcal{M}$, is deformed in order to match the pre-segmentation borders more accurately. In (15), the external force definition is important as it allows driving the mesh to the image's natural edges. Its computation is achieved by using the normal profile to each vertex, in a way similar to Active Shape Models (Cooper et al., 1995; Weese et al., 2001). However, as reported in this paper, an elastically deformable model is used, avoiding the need for a training set. A set of sampling points is defined over each normal profile of length $2l$ as:

$$x_{i,j} = P_i + j\delta\overrightarrow{N_i} \quad (18)$$

where δ is a sampling distance, and $j = \{[-l/\delta], [-l/\delta]+1, \ldots, [l/\delta]-1, [l/\delta]\}$. Figure 7 shows the normal profiles for a specific mesh. A target point, x_i^{target}, defined as the first point inside the mask, M_3, is searched in each profile, starting from l to $-l$. Thus, using the target point, the external force, $\overrightarrow{F_{ext_i}}$ is defined in each vertex as:

$$\overrightarrow{F_{ext_i}} = \left[\frac{\nabla M_3(x_i^{target})}{\left\|\nabla M_3(x_i^{target})\right\|} \cdot \left(x_i^{target} - P_i\right)\right]\overrightarrow{N_i} \quad (19)$$

where $\nabla M_3(x_i^{target})$ is the gradient of M_3 at x_i^{target}, i.e., the gradient of the mask border. In this way, the vertex is pushed to the pre-segmentation border more strongly if the normal of the mask border is in the same direction as the mesh normal.

Because an affine transformation was used in the previous mesh geometric adjustment, it can be assumed that the mesh

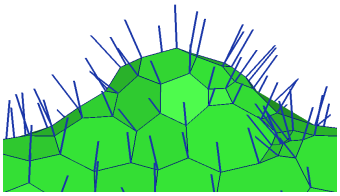

Figure 7: Profiles normal to the mesh surface at each vertex. The measures of the image gray level used to guide the mesh deformation are taken along these profiles.

did not lose its general shape. Therefore, to avoid an excessive mesh deformation if there are errors in the pre-segmentation, the initial simplex angles of the mesh are preserved as target simplex angles, ρ_i^* during the deformation. Thus, the simplex angle of every vertex, ρ_i is computed after the geometric adjustment and used in this deformation as ρ_i^* (Eq. 17). An example of the adjustment result to the pre-segmentation is shown in Figure 5(b).

2.2.3.3. Second Mesh Deformation.

The second deformation is computed using the original MRI, and its goal is to find the GM-CSF interface.

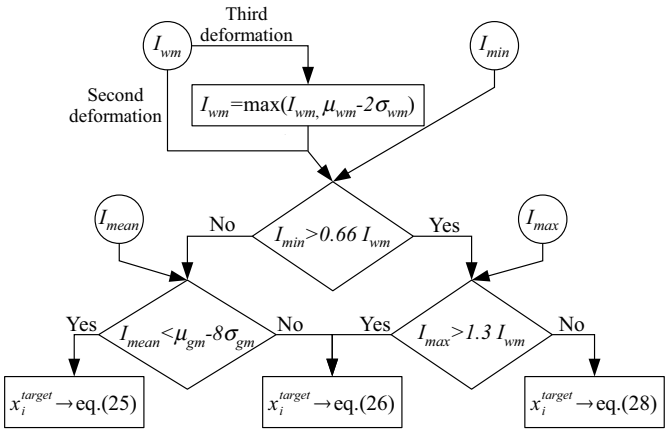

Figure 8: Flow diagram of the rules to compute the simplex mesh external forces. The inputs, represented by circles, are measures of the image gray level taken over the normal profile of each vertex (Fig. 7). The outputs, at the end of the diagram, are the equations used to compute the target point, x_i^{target} of each vertex.

In a similar manner to the first deformation, a target point, x_i^{target} is computed in each vertex profile. (See (18)). To compute the target point, rules based on the image gray level are applied, as will be explained later in this section (Fig. 8). In each iteration, the vertices are pushed toward their target points by the external force. To accomplish this, the external force, $\overrightarrow{F_{ext_i}}$ is computed using the target points and including an exponential decay if the target point is further than a distance, D_F:

$$\overrightarrow{F_{ext_i}} = \left(x_i^{target} - P_i\right)\beta \tag{20}$$

where,

$$\beta = \begin{cases} 1, & \text{if } \left\|x_i^{target} - P_i\right\| < D_F \\ \frac{1}{\exp\left(\left\|x_i^{target} - P_i\right\| - D_F\right)}, & \text{if } \left\|x_i^{target} - P_i\right\| \geq D_F \end{cases} \tag{21}$$

Figure 8 shows a flow diagram of the rules employed to compute the target points. First, whether the vertex P_i is outside the WM is estimated. This is carried out by computing two values: an estimation of the WM gray value in each profile

$$I_{wm}(i) = \max_{j=[-l/\delta],\ldots,0} I(x_{i,j}), \tag{22}$$

and the minimum gray level value over a distance, d_{min} in the direction, $-\overrightarrow{N_i}$:

$$I_{min}(i) = \min_{j=[-d_{min}/\delta],\ldots,0} I(x_{i,j}) \tag{23}$$

If $I_{min}(i) \leq 0.66\ I_{wm}(i)$, it is assumed that the vertex, P_i is in the CSF or the GM. In this case, another measurement is made over a distance, d_{mean} in the direction, $-\overrightarrow{N_i}$:

$$I_{mean}(i) = \frac{\sum_{j=[-d_{mean}/\delta]}^{0} I(x_{i,j})}{[d_{mean}/\delta] + 1} \tag{24}$$

Using $I_{mean}(i)$, it is possible to determine whether the vertex, i, is near the GM. If $I_{mean}(i)$ has a low value, the vertex, i, is in the CSF far from the GM. In this case, P_i must be pushed to reach the GM. $I_{mean}(i)$ is analyzed using the mean value μ_{gm} and standard deviation σ_{gm} of the GM gray level computed in section 2.1.3. Accordingly, if $I_{mean}(i) < \mu_{gm} - 8\sigma_{gm}$, the vertex is pushed inward. Since each vertex is pushed over its target point, the target point is defined as:

$$x_i^{target} = P_i - d_p\overrightarrow{N_i} \tag{25}$$

where d_p is a distance that controls the applied force. Otherwise, if $I_{mean}(i) \geq \mu_{gm} - 8\sigma_{gm}$, it is assumed that the vertex is near the interface between the GM and CSF, and must be pushed into it. This interface can be detected looking for a high gradient in the search profile. A function, $\mathcal{F}$, based on both image and mesh, is defined as $\mathcal{F}_i(x) = -\overrightarrow{N_i} \cdot \nabla I(x)$, where $I(x)$ is the gray value of the image normalized between the values [0,1] at point x, and ∇ is the gradient operator. Then, the target point (Weese et al., 2001) is defined as:

$$x_i^{target} = P_i + \underset{j=[-l/\delta],\ldots,[l/\delta]}{\arg\max} \left[\mathcal{F}_i(x_{i,j}) - Dj^2\delta^2\right]\delta\overrightarrow{N_i} \tag{26}$$

where D is a weight to give less importance to points that are far from P_i. In contrast, if $I_{min}(i) > 0.66\ I_{wm}(i)$, it is assumed that the vertex P_i is inside the WM. In this case, another measure is performed over a distance, d_{max}, in the profile:

$$I_{max}(i) = \max_{j=0,\ldots,[d_{max}/\delta]} I(x_{i,j}) \tag{27}$$

The purpose of $I_{max}(i)$ is to determine whether the eyes are in front of $P(i)$. An area with high gray level values characterizes the region behind the eyes, where the optic tracts are located. We estimated a threshold for $I_{max}(i)$ to be 130% of the WM intensity. If $I_{max}(i) > 1.3\ I_{wm}$, it is assumed that the eyes are in front of P_i, and the GM border is found using (26); otherwise, the vertex P_i is inside the WM and must be pushed to reach the GM and

the GM-CSF interface. The vertex is pushed defining the target point x_i^{target} as:

$$x_i^{target} = P_i + d_p \overrightarrow{N_i} \tag{28}$$

In the second deformation, the mesh should be adjusted more precisely. Therefore, it is allowed more freedom in the deformation by defining the target simplex angle, ρ_i^*, using a curvature continuity constraint (Delingette, 1999) computed over a neighborhood, $Q^S(i)$, of size, S, around each vertex. The neighborhood, $Q^S(i)$, is defined as all the vertices that can be connected to P_i by a path formed with S edges. Figure 5(c) shows an example of the mesh obtained after the second deformation.

The pre-segmentation is designed to eliminate the non-brain tissue to be able to find landmarks to register the generic mesh, $\mathcal{M}$, with the image (sec. 2.2.2), but in some cases part of the brain is also removed. Therefore, the purpose of the second deformation, in addition to reaching the GM-CSF interface, is to correct the mesh in those areas where the pre-segmentation eliminated brain tissue. Figure 9 shows an example in which part of the brain was removed in the pre-segmentation and recovered in the second deformation.

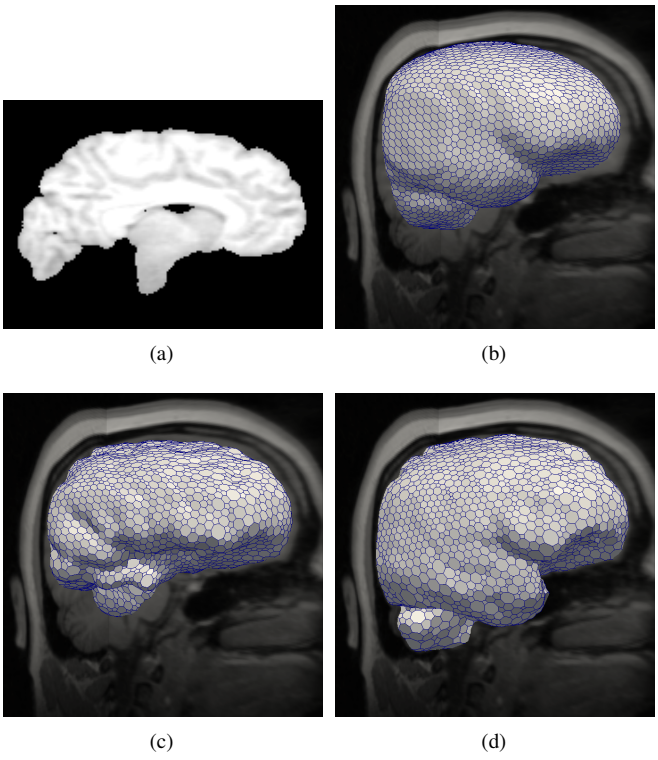

Figure 9: Example of brain tissue recovery by the second deformation. (a) The pre-segmentation of an image in which the cerebellum has been removed because of a bias problem in the image. (b) Mesh registered with the pre-segmentation by geometric transformations. (c) Mesh deformed using the pre-segmented image. This first deformation removes a great part of the cerebellum because it is based in the pre-segmentation. (d) Mesh after the second deformation. This deformation recovers the cerebellum because the forces that push the vertices if they are inside the brain tissue.

2.2.3.4. Third Mesh Deformation.

A final deformation is carried out removing parts of the CSF that may remain outside the cortex or in the sulci, by mesh refinement, and using similar forces to those described in the previous section. There are many well-known algorithms to refine triangulations. Therefore, the simplex mesh is first transformed into a triangulation using the method described in (Galdames and Jaillet, 2010). This method is based on the computation of the dual mesh vertices by an interpolation that uses a direct minimization of the distance to both vertices of each face and the tangent planes in these vertices. After the dual transformation, the triangulation is refined using the butterfly scheme (Zorin et al., 1996), and re-transformed into a simplex mesh (Galdames and Jaillet, 2010). To deform the refined mesh, similar forces to those described in the previous section (sec 2.2.3.3) are utilized. The difference is that the value of $I_{wm}(i)$ is modified if it is very different from the estimation of the WM gray level in the pre-segmentation stage. The objective of this correction is to make sure that vertices over sulci will be pushed into the sulci. There are cases in which the estimation of the WM local gray level $I_{wm}(i)$ is excessively low when the vertex is over a large sulcus, especially over the sagittal sinus. Moreover, in this stage the mesh has reached the cortex as a result of the second deformation; therefore, it is more important to push the vertices into the sulcus. If $I_{wm}(i) < \mu_{wm} - 2\sigma_{wm}$, its value is replaced by $I_{wm}(i) = \mu_{wm} - 2\sigma_{wm}$. Figure 5(d) shows an example of the final segmentation.

2.2.3.5. Mesh Self-intersections Control.

Mesh deformations following complex shapes such as cortex sulci and gyri, may generate errors due to mesh self-intersections. A self-intersection may cause the surface normal vector to point toward inside the mesh instead of outward. This error in the normal vector causes the mesh to be pushed in the wrong direction, because the forces that deform the mesh depend on the surface normal vector. The mesh internal forces avoid these intersections to some degree, but in some cases they are not sufficient.

To prevent these self-intersections, their occurrence is checked and corrected every $\mathcal{I} = 10$ iterations. The vertices that form a face of a simplex mesh are not co-planar; therefore, there are no planes available to compute the intersections easily. Consequently, the simplex mesh is first transformed into its dual triangulation (Galdames and Jaillet, 2010) to have a mesh formed by planar faces. Then, the intersections between triangles can be computed easily. Because the topological dual triangulation is used, each triangle corresponds to a vertex of the simplex mesh (Fig. 6(c)). Therefore, if an intersection is detected in a triangle, the position of the corresponding simplex mesh vertex must be corrected. After all triangles with intersections have been detected, areas enclosed by these triangles are computed. The triangles of these areas have completely crossed a part of the mesh. Therefore, the position of the simplex mesh vertices related to triangles in the enclosed areas must also be corrected.

Consequently a set, $\mathcal{G}$, is formed with the vertices related to intersected triangles and triangles enclosed by intersections. To correct the intersections, a Laplacian smoothing is applied to the vertices of $\mathcal{G}$ and to a neighborhood around them. The smoothing is applied in stages $k = \{1, 2, \dots\}$ to make sure of

the self-intersection problem correction, while changing the rest of the mesh as little as possible . In each stage, the Laplacian smoothing is applied 50 times or until the mean displacement of the vertices is less than 0.001.

Another detection of self-intersections and enclosed areas is performed at the end of each stage. If there are still self-intersections, another set ,$\mathcal{G}$, is formed in the next stage and a Laplacian smoothing is carried out. The neighborhood around $\mathcal{G}$ depends on the stage, k, defining increasing neighborhoods to provide more freedom if the intersections were not corrected in the previous stage. Thus, in a stage k, the neighborhood $Q^S(\mathcal{G})$ of $\mathcal{G}$ is of size $S = k$, where $Q^S(\mathcal{G})$ is defined as all the vertices that can be connected to any vertex of $\mathcal{G}$ by a path formed with S edges.

3. Databases and Experiments

For the purpose of measuring the performance of our proposed SMHASS method, we use the most commonly used MRI databases:

- 20 simulated T1W MRI images from the BrainWeb website (Cocosco et al., 1997; Aubert-Broche et al., 2006), with 1mm isotropic voxel size. This database has the ground truth segmentations for 12 tissues available, including GM, WM and CSF.
- 18 real T1W MRI images from the Internet Brain Segmentation Repository (IBSR) (Center for Morphometric Analysis, 1995), slice thickness 1.5 mm. This database has a manual segmentation of the GM, WM and CSF available.
- 40 real T1W MRI images from the Segmentation Validation Engine (SVE) (Shattuck et al., 2009) website, with 1.5 mm slice thickness and in-plane voxel resolution of 0.86 mm (38 subjects) or 0.78 mm (2 subjects). There are no ground truth segmentations available for this data set. However, segmentation masks can be sent to the website for performing an online comparison with manually edited brain mask volumes.

Our SMHASS method was validated by comparing its performance with that of three of the best methods in the literature. These methods are:

The Brain Extraction Tool (BET) (Smith, 2002) that segments the brain using deformable models. The image is binarized using estimations of the minimum and maximum intensities of the brain. Next, the center of the head is estimated in the binarized image and the deformable model is initialized with a sphere shape in this position. The model is deformed using locally adaptive forces. BET v2.1 is free and available in the FMRIB FSL software library (FMRIB). The recommended default parameters were used for the evaluation: fractional intensity threshold = 0.5, threshold gradient = 0.

The Brain Surface Extractor (BSE) method (Shattuck et al., 2001) uses Marr-Hildreth edge detection to identify the border of the brain. Before applying the edge detector, anisotropic diffusion filtering (Perona and Malik, 1990) is used to de-noise the image. This spatially adaptive filter smoothes noisy regions while preserving edge boundaries. After applying the edge detection, the image is binarized using the computed edges, and the brain is found using morphological operators. Binary erosion is applied to separate the elements and a 3D connected component analysis is carried out to identify the brain. Next, a morphological dilation is applied to the selected element (brain) to undo the effects of the erosion, and a closing operation is performed to close the small holes that may be in the volume. BSE is freely available as part of the BrainSuit (BrainSuite) of the Laboratory of Neuro Imaging (LONI) at UCLA. Two sets of parameters were used in our evaluations: the default parameters (diffusion iterations = 3, diffusion constant = 25, edge constant = 0.64, erosion size = 1), and the parameters suggested by Hartley et al (Hartley et al., 2006; Sadananthan et al., 2010) (diffusion iterations = 3, diffusion constant = 35, edge constant = 0.62, erosion size = 2).

The Hybrid Watershed Algorithm (HWA) (Ségonne et al., 2004) is a hybrid method that combines a watershed algorithm (Hahn and Peitgen, 2000), and a deformable surface model (Dale et al., 1999) which includes shape restrictions based on an atlas. First, a watershed algorithm that uses the concept of pre-flooding (the connectivity path between two points can contain a lower intensity than the darker of the two points up to a maximum difference) is used to segment the brain. Then, the deformable model is initialized with a balloon shape using this segmentation. A first deformation of the model is carried out using the watershed segmentation and global parameter estimations. Next, an atlas is used to verify the resulting surface and correct it if there are errors. Finally, a deformation using estimations of local parameters is performed to find the brain borders. HWA v5 is included in the FreeSurfer software package (FreeSurfer) developed at the Martinos Center for Biomedical Imaging. The default parameters and the "-atlas" option to use basic atlas information to correct the result of the deformations, were used in our tests. The default parameters are: weight for the atlas = 0.85; probability of merging = 0.32; pre-flooding height = 10; seed points using atlas information; template deforming using atlas information; use of pre-weighting for the template deformation.

The parameters used to segment the three databases with our SMHASS method were as follows: The parameters for the first mesh deformation using deformable models were: $\lambda = 0.8$, $\beta = 0.3$, $\gamma = 0.65$, $\delta = 0.5$, $l = 15$ and $D_F = 10$. The parameters for the second and third mesh deformations were: $\lambda = 0.6$, $\beta = 0.4$, $\gamma = 0.3$, $S = 2$, $\delta = 0.5$, $l = 8$, $d_{min} = 4$, $D = 0.3$, $d_{max} = 5$, $d_{mean} = 2$, $d_p = 0.5$ and $D_F = 1$. To validate and compare the SMHASS method, a binary mask was built using the final mesh after segmentation.

The two volumetric measures most used in the literature to compare the quality of skull stripping methods were employed: the Jaccard similarity (Jaccard, 1912) and the Dice coefficient (Dice, 1945). These volumetric measures can be computed using the concepts of True Positive (TP), False Positive (FP), True Negative (TN) and False Negative (FN). In our case the TP and FP are defined as the number of voxels correctly and incorrectly classified as brain tissue, respectively. Similarly, TN and FN are defined as the number of voxels correctly and

incorrectly classified as non-brain tissue, respectively. The Jaccard similarity, also termed the Tanimoto coefficient, measures the similarity of two sets, S_1, S_2, as the ratio of the size of their intersection divided by the size of their union:

$$J(S_1, S_2) = \frac{|S_1 \cap S_2|}{|S_1 \cup S_2|} = \frac{TP}{TP + FP + FN} \tag{29}$$

The Dice coefficient measures the similarity of two sets, S_1, S_2, as the ratio of twice the size of their intersection divided by the sum of their sizes:

$$\kappa(S_1, S_2) = \frac{2\,|S_1 \cap S_2|}{|S_1| + |S_2|} = \frac{2TP}{2TP + FP + FN} \tag{30}$$

the Dice coefficient is related to the Jaccard similarity by:

$$\kappa = \frac{2J}{J + 1} \tag{31}$$

The sensitivity and specificity percentages were also computed, which show the percentage of brain and non-brain voxels recognized respectively:

$$\begin{aligned} \text{Sensitivity} &= \frac{TP}{TP + FN} \\ \text{Specificity} &= \frac{TN}{TN + FP} \end{aligned} \tag{32}$$

4. Results

In the BrainWeb and IBSR databases, the ground truth was the union of GM and WM using the available segmentations. Tables 1 and 2 show the performance of the different segmentation methods using the BrainWeb and IBSR databases, respectively. In the SVE database, the ground truth is not available, but the segmentation can be evaluated by an independent online assessment that provides all used volumetric measurements. Additionally, the performance of the other methods is available online for this database. Table 3 shows the performance of the methods in the SVE database. In addition to the segmentations using the methods default parameters, segmentation performances with different parameters can be found on the SVE website. The segmentation results with better performance for each method are also shown in Table 3 marked with an *. Furthermore, an additional result of our SMHASS method is shown in Table 3, in which the output was dilated using a structural element of 3x3x3mm (3x3x3voxels). The performance of the dilated masks was better, but this improvement only ocurred in the SVE database.

Figures 10 and 11 show a comparison among different segmentations of a BrainWeb and IBSR image, respectively. Figure 10 also includes an image of the ground truth segmentation, and a zoom of the cortex for better comparison. The HWA has a low specificity in both databases (see Table 2 and 3), nevertheless, the specificity of BSE is lower in the IBSR database when the default parameters are used (Fig. 11(d)). Also, the specificity of BET is low in the BrainWeb database (Fig. 10(d)) obtaining a low overall performance even though its sensitivity is good. The best performance was obtained by our SMHASS method (Figs 10(g) and 11(f)), followed by BSE in the BrainWeb database; BET in the IBSR database; and BSE.0.8b and BETv2.1 in the SVE database.

Figures 12 and 13 are provided by the SVE website and show the projections of FN and FP of the best result obtained by each method in the SVE database (methods marked with an * in Table 3). In the same way as in the other databases, the HWA has the lowest specificity with a high number of FP (Fig. 13(a)). Conversely, the HWA has the highest sensitivity with very few FN (Fig. 12(a)). Nevertheless, it has the worst overall performance (Jaccard and Dice in Table 3). The best performance is obtained by our SMHASS method if a dilatation is applied to the segmentation mask (Figs. 12(e) and 13(e)). It can be observed that the SMHASS method has the lowest sensitivity (Fig. 12(d)) and the highest specificity (Fig. 13(d)) before dilatation; however, after dilation these values improve obtaining the best overall performance.

An analysis of variance (ANOVA) and post hoc comparisons were used to verify the statistical significance ($p < 0.05$) of the differences among the results (Jaccard and Dice) of our SMHASS method and those of others. The Games-Howell method, that assumes that population variances may be different, was used for the post hoc comparisons. Using the union of the results obtained in the BrainWeb and IBSR databases for comparison, SMHASS has a statistically significant difference with respect to the others. Also, the difference is statistically significant if the segmentation results in the BrainWeb and IBSR databases are used together with the results obtained with the default parameters in the SVE database. The difference is not statistically significant with only the BSEv0.8b* method if all the results for the SVE database are taken into account.

5. Conclusions

Skull stripping methods are designed to eliminate non-brain tissue in magnetic resonance (MR) brain images. This is a fundamental step for enabling processing of brain MR images. The aim of this study was to develop a new skull stripping method based on two steps: the first one a pre-segmentation that employs thresholds and morphological operators; and the second step a segmentation based on deformable models. The pre-segmentation is built on previous work but incorporates new estimations of the optimal thresholds, based on comparisons with a brain atlas. This pre-segmentation makes it possible to find an optimal initialization for the deformable model, providing robustness to the segmentation. The deformable model is based on a simplex mesh, and its deformation is guided by local image gray levels, and a gray level statistical model constructed on the pre-segmentation. The deformation is based on 3 steps which make it possible to use the pre-segmentation to find the optimal starting point for the deformation; to recover brain tissue ignored in the pre-segmentation and; to decrease the amount of CSF and sub-arachnoid space in the segmentation. The result of these steps is an accurate segmentation that minimizes the amount of non-brain tissue, without losing brain parenchyma.

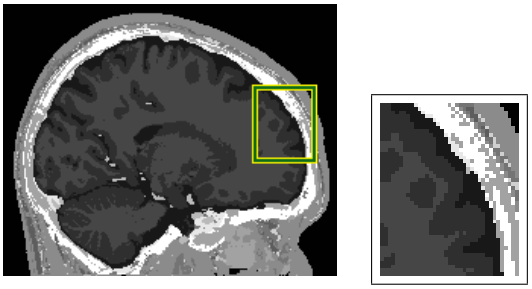

(a) Model

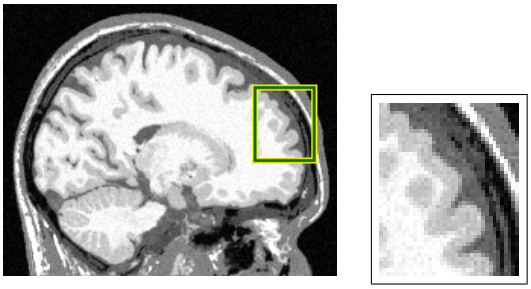

(b) Original

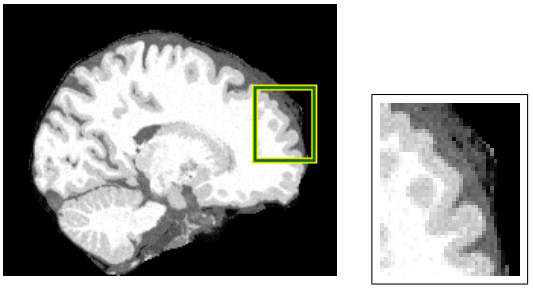

(c) HWA

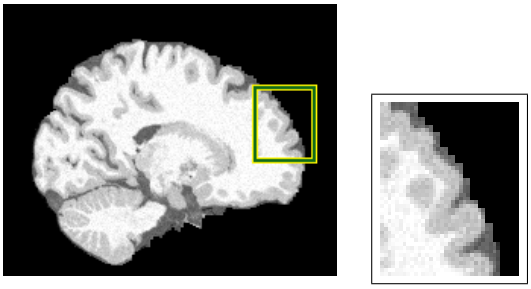

(d) BET

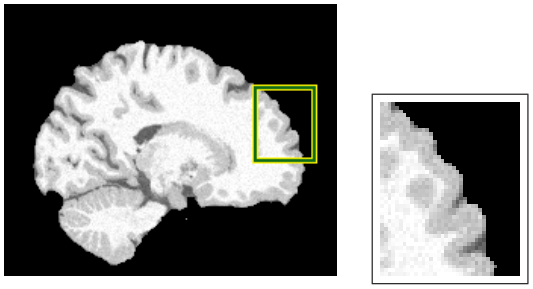

(e) BSE (default)

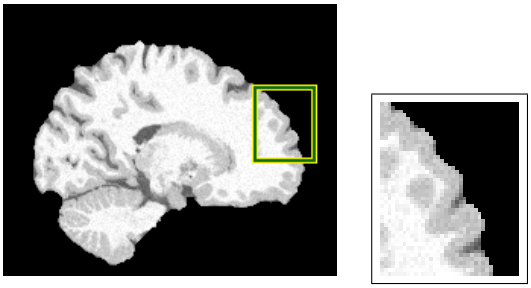

(f) BSE (Hartley)

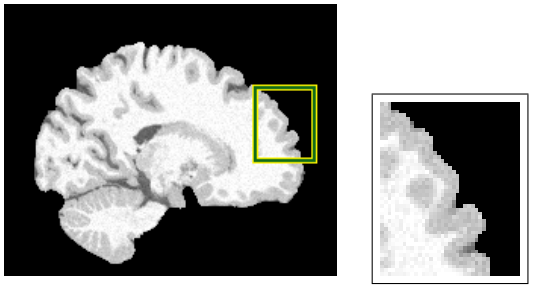

(g) SMHASS

Figure 10: Comparison among different automatic segmentations of an image of the BrainWeb database (b). (a) Shows the ground truth segmentation with a marked zoom rectangular area. It can be seen that the HWA (c) is the method that leaves most non-brain tissue, mainly CSF. For this reason the HWA has the lowest specificity among the methods. The HWA has the highest sensitivity, because most of the brain tissue is included in the segmentation. Nevertheless, its overall performance (Jaccard and Dice) is lower than that of the other methods. The best performance was obtained by our SMHASS method (g), which also has the highest specificity, followed by the BSE using Hartleys parameters.

Table 1: Performance Comparison among Different Methods using the BrainWeb database (Cocosco et al., 1997; Aubert-Broche et al., 2006). The best results are shown in bold.

Method	Jaccard mean (SD)	Dice mean (SD)	Sensitivity mean (SD)	Specificity mean (SD)
BET2.1	0.812 (0.020)	0.896 (0.012)	0.997 (0.002)	0.964 (0.004)
BSE (def.)	0.823 (0.091)	0.900 (0.061)	0.995 (0.003)	0.964 (0.027)
BSE (Hard.)	0.875 (0.049)	0.932 (0.031)	0.991 (0.004)	0.979 (0.012)
HWA	0.685 (0.017)	0.813 (0.012)	**1.000** (0.001)	0.928 (0.005)
SMHASS	**0.903** (0.010)	**0.949** (0.006)	0.984 (0.004)	**0.986** (0.002)

Table 2: Performance Comparison among Different Methods using the IBSR database (Center for Morphometric Analysis, 1995). The best results are shown in bold.

Method	Jaccard mean (SD)	Dice mean (SD)	Sensitivity mean (SD)	Specificity mean (SD)
BET2.1	0.882 (0.092)	0.935 (0.06)	0.985 (0.012)	0.982 (0.019)
BSE (def.)	0.749 (0.152)	0.848 (0.101)	0.988 (0.011)	0.941 (0.049)
BSE (Hard.)	0.848 (0.065)	0.916 (0.038)	0.945 (0.072)	0.984 (0.014)
HWA	0.814 (0.036)	0.897 (0.022)	**1.000** (0.000)	0.966 (0.012)
SMHASS	**0.895** (0.067)	**0.943** (0.039)	0.920 (0.079)	**0.996** (0.004)

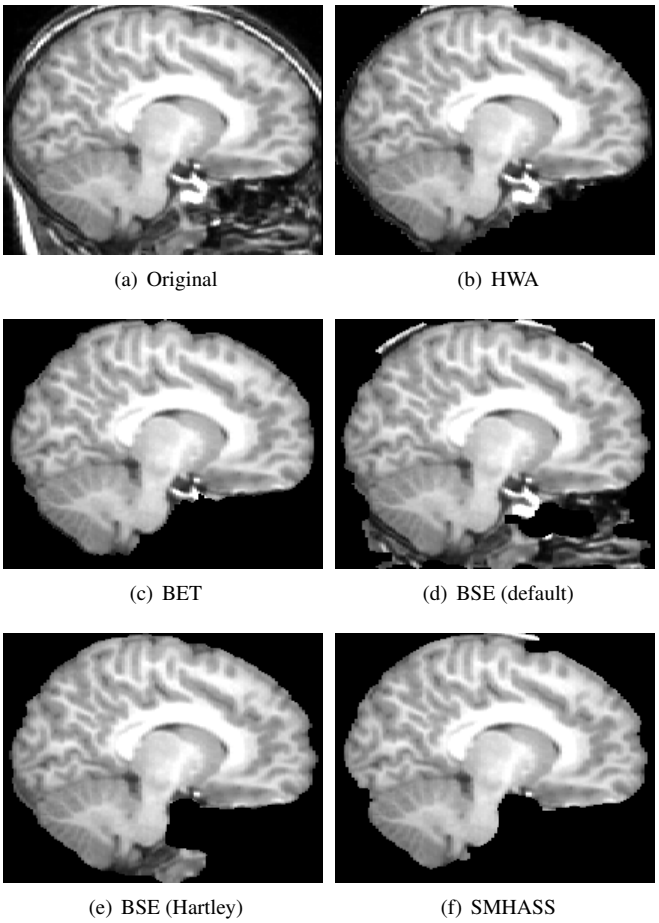

(a) Original (b) HWA

(c) BET (d) BSE (default)

(e) BSE (Hartley) (f) SMHASS

Figure 11: Comparison among different automatic segmentations of an image from the IBSR database (a). The BSE method has the lowest specificity when the default parameters are used (d). The HWA (b) also has a low specificity but its sensitivity is better, obtaining better overall performance. Although the performance of BSE rises considerably when Hartley's parameters are used (e), does not exceed the BET performance (c). Nevertheless, our SMHASS method (f) has better performance than BET.

Our Simplex Mesh and Histogram Analysis Skull Stripping, SMHASS, method was tested using international MRI databases available on the web: the BrainWeb, the Internet Brain Segmentation Repository (IBSR), and the Segmentation Validation Engine (SVE). We compared our method's performance to that of three of the most popular methods in the literature: the Brain Extraction Tool (BET), the Brain Surface Extractor (BSE), and the Hybrid Watershed Algorithm (HWA). Performance was measured using the Jaccard Index (J) and Dice Coefficient (κ). Our method achieved the best performance and the difference was statistically significant ($p < 0.05$): J=0.903 and κ=0.949, on BrainWeb; J=0.895 and κ=0.943 on IBSR; J=0.948 and κ=0.973 on SVE. The obtained segmentations were accurate along all databases, and the performance variance was low. Incorporating this skull stripping method in a future method to segment the whole brain anatomy is an expectation for future work.

Acknowledgements

This work was partially funded by the Department of Electrical Engineering, Universidad de Chile, and Fondef grant, D08I1060. Also, this work was carried out within the PLOMO project, a French-South American cooperation that aims to develop an integrated software platform dedicated to the medical modeling field, and the authors would like to thank all the members of this project for their remarks, testing, and evaluation of the final meshes (PLOMO).

Ashburner J, Friston KJ. Voxel-based morphometry-the methods. NeuroImage 2000;11(6):805–21.

Atkins MS, Mackiewich BT. Fully automatic segmentation of the brain in MRI. IEEE Trans on Medical Imaging 1998;17(1):98–107.

Aubert-Broche B, Evans AC, Collins L. A new improved version of the realistic digital brain phantom. NeuroImage 2006;32(1):138–45.

Baillard C, Hellier P, Barillot C. Segmentation of brain 3D MR images using level sets and dense registration. Medical Image Analysis 2001;5(3):185–94.

de Boer R, Vrooman HA, Ikram MA, Vernooij MW, Breteler MM, van der Lugt A, Niessen WJ. Accuracy and reproducibility study of automatic mri brain tissue segmentation methods. NeuroImage 2010;51(3):1047–56.

Table 3: Performance Comparison among Different Methods using the SVE database (Shattuck et al., 2009). The results marked with * are the best on the website for each method, and the parameters used for these segmentations are given below the table. Best results are shown in bold.

Method	Jaccard mean (SD)	Dice mean (SD)	Sensitivity mean (SD)	Specificity mean (SD)
BETv2.1	0.892 (0.054)	0.942 (0.032)	0.986 (0.006)	0.980 (0.014)
BETv2.1*	0.940 (0.009)	0.969 (0.005)	0.962 (0.012)	**0.996** (0.001)
BSEv08a (def.)	0.596 (0.207)	0.727 (0.150)	0.980 (0,014)	0.854 (0.094)
BSEv08b*	0.943 (0.028)	0.970 (0.016)	0.975 (0.033)	0.994 (0.002)
HWA3	0.851 (0.019)	0.919 (0.011)	0.999 (0.000)	0.969 (0.006)
HWA3*	0.854 (0.018)	0.921 (0.011)	**0.999** (0.000)	0.969 (0.005)
SMHASS	0.917 (0.016)	0.957 (0.009)	0.928 (0.019)	0.998 (0.001)
SMHASS (dilatation)	**0.948** (0.010)	**0.973** (0.005)	0.986 (0.005)	0.993 (0.003)

parameters for BSEv08b*: -n 5 -d 15 -s 0.65 -p –noneck
parameters for BETv2.1*: -B
parameters for HWA3*: -less

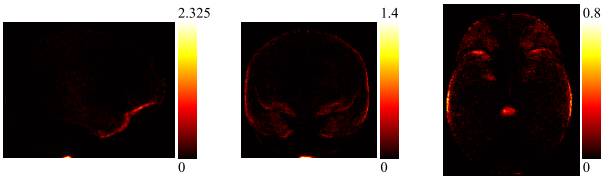

(a) HWA3*

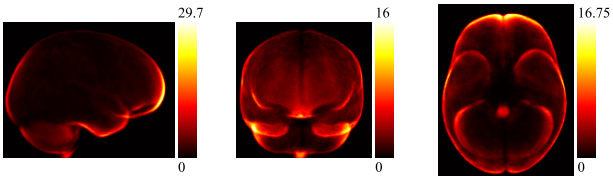

(b) BETv2.1*

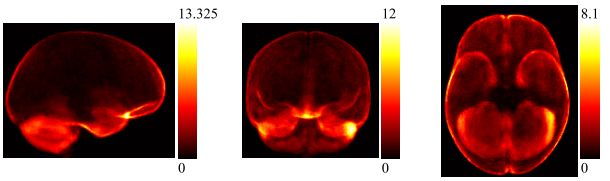

(c) BSEv0.8b*

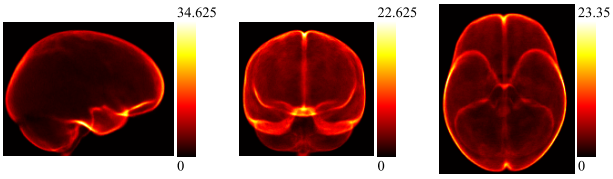

(d) SMHASS

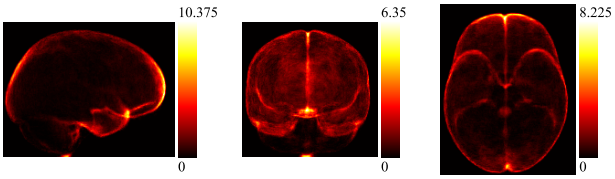

(e) SMHASS dilated

Figure 12: Projections of the FN provided by the SVE website. The FN projections of the different methods best segmentation results are shown (see Table 3). The methods shown in this figure are: HWA3*, BSEv0.8b*, BSEv0.8b*, and our SMHASS method with and without dilatation. The color scale represents the sum of the FN along the direction orthogonal to the figure plane.

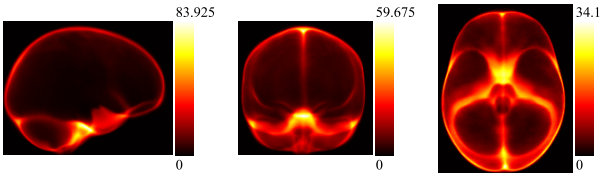

(a) HWA3*

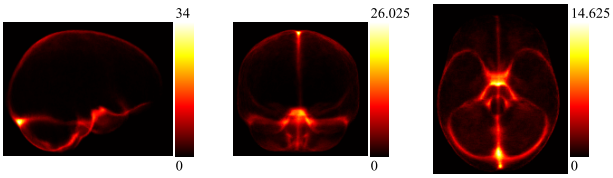

(b) BETv2.1*

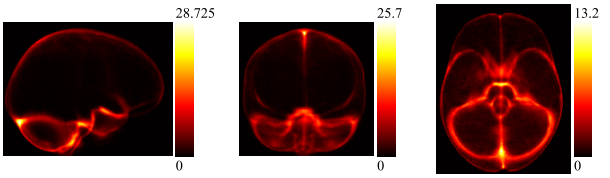

(c) BSEv0.8b*

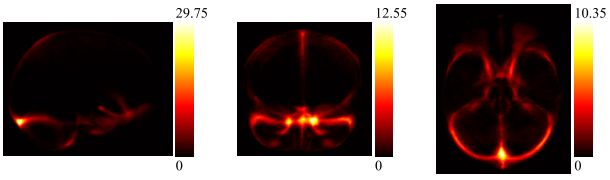

(d) SMHASS

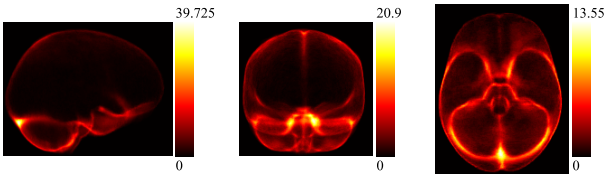

(e) SMHASS dilated

Figure 13: Projections of the FP provided by the SVE website. The FP projections for best segmentation results obtained by the different methods are shown (see Table 3). The showed methods are: HWA3*, BSEv0.8b*, BSEv0.8b*, and our SMHASS method with and without dilatation. The color scale represents the sum of the FP along the direction orthogonal to the figure plane.

Boesen K, Rehm K, Schaper K, Stoltzner S, Woods R, Lüders E, Rottenberg D. Quantitative comparison of four brain extraction algorithms. NeuroImage 2004;22(3):1255–61.

Böttger T, Kunert T, Meinzer HP, Wolf I. Application of a new segmentation tool based on interactive simplex meshes to cardiac images and pulmonary MRI data. Academic Radiology 2007;14(3):319–29.

BrainSuite . Laboratory of Neuro Imaging (LONI), UCLA. http://www.loni.ucla.edu/Software/BrainSuite.

Carass A, Cuzzocreo J, Wheeler MB, Bazin PL, Resnick SM, Prince JL. Simple paradigm for extra-cerebral tissue removal: Algorithm and analysis. NeuroImage 2011;56(4):1982–92.

Center for Morphometric Analysis . Massachusetts General Hospital, The Internet Brain Segmentation Repository (IBSR). 1995. http://www.cma.mgh.harvard.edu/ibsr/.

Chiverton J, Wells K, Lewis E, Chen C, Podda B, Johnson D. Statistical morphological skull stripping of adult and infant MRI data. Computers in Biology and Medicine 2007;37:342–57.

Cocosco CA, Kollokian V, Kwan RKS, Evans AC. Brain web: Online interface to a 3D MRI simulated brain database. NeuroImage 1997;5(4):425–.

Cooper D, Cootes T, Taylor C, Graham J. Active shape models - their training and application. Computer Vision and Image Understanding 1995;61:38–59.

Cox RW. AFNI: software for analysis and visualization of functional magnetic resonance neuroimages. Computers and Biomedical Research 1996;29(3):162–73.

Dale AM, Fischl B, Sereno MI. Cortical surface-based analysis: I. segmentation and surface reconstruction. Neuroimage 1999;9(2):179–94.

Delingette H. General object reconstruction based on simplex meshes. Int J of Computer Vision 1999;32(2):111–46.

Dice LR. Measures of the amount of ecologic association between species. Ecology 1945;26(3):297–302.

Dogdas B, Shattuck DW, Leahy RM. Segmentation of skull and scalp in 3-D human MRI using mathematical morphology. Human Brain Mapping 2005;26(4):273–85.

Fennema-Notestine C, Ozyurt IB, Clark CP, Morris S, Bischoff-Grethe A, Bondi MW, Jernigan TL, Fischl B, Segonne F, Shattuck DW, Leahy RM, Rex DE, Toga AW, Zou KH, BIRN M, Brown GG. Quantitative evaluation of automated skull-stripping methods applied to contemporary and legacy images: Effects of diagnosis, bias correction, and slice location. Human Brain Mapping 2006;27(2):99–113.

FMRIB . Software library of the Oxford Centre for Functional MRI of the Brain (FMRIB). http://www.fmrib.ox.ac.uk/fsl/.

FreeSurfer . Software package developed at the Martinos Center for Biomedical Imaging. http://surfer.nmr.mgh.harvard.edu/.

Galdames F, Jaillet F. From Triangulation to Simplex Mesh: a Simple and Efficient Transformation. Technical Report RR-LIRIS-2010-021; LIRIS UMR 5205 CNRS/INSA de Lyon/Université Claude Bernard Lyon 1/Université Lumire Lyon 2/École Centrale de Lyon; 2010.

Galdames FJ, Perez CA, Estévez PA, Held CM, Jaillet F, Lobo G, Donoso G, Coll C. Registration of renal SPECT and 2.5D US images. Computerized Medical Imaging and Graphics 2011;35(4):302–14.

Gilles B, Magnenat-Thalmann N. Musculoskeletal MRI segmentation using multi-resolution simplex meshes with medial representations. Medical Image Analysis 2010;14(3):291–302.

Grau V, Mewes A, Alcañiz M, Kikinis R, Warfield S. Improved watershed transform for medical image segmentation using prior information. IEEE Trans on Medical Imaging 2004;23(4):447–58.

Hahn HK, Peitgen HO. The skull stripping problem in MRI solved by a single 3D watershed transform. In: Third International Conference on Medical Image Computing and Computer-Assisted Intervention (MICCAI). Springer; 2000. p. 134–43.

Hartley S, Scher A, Korf E, White L, Launer L. Analysis and validation of automated skull stripping tools: a validation study based on 296 MR images from the Honolulu Asia aging study. NeuroImage 2006;30(4):1179–86.

Huang A, Abugharbieh R, Tam R, Traboulsee A. MRI brain extraction with combined expectation maximization and geodesic active contours. In: IEEE International Symposium on Signal Processing and Information Technology. 2006. p. 394–7.

Hwang J, Han Y, Park H. Skull-stripping method for brain MRI using a 3D level set with a speedup operator. J of Magnetic Resonance Imaging 2011;34(2):445–56.

Iglesias JE, Liu CY, Thompson P, Tu Z. Robust brain extraction across datasets and comparison with publicly available methods. IEEE Trans on Medical Imaging 2011;doi: 10.1109/TMI.2011.2138152.

Jaccard P. The distribution of the flora in the alpine zone. New Phytologist 1912;11(2):37–50.

Jenkinson M, Pechaud M, Smith S. BET2: MR-based estimation of brain, skull and scalp surfaces. In: Eleventh Annual Meeting of the Organization for Human Brain Mapping. 2005. .

Kapur T, Grimson WEL, III WMW, Kikinis R. Segmentation of brain tissue from magnetic resonance images. Medical Image Analysis 1996;1(2):109–27.

Klein A, Ghosh SS, Avants B, Yeo B, Fischl B, Ardekani B, Gee JC, Mann J, Parsey RV. Evaluation of volume-based and surface-based brain image registration methods. NeuroImage 2010;51(1):214–20.

Kovacevic N, Lobaugh NJ, Bronskill MJ, Levine B, Feinstein A, Black SE. A robust method for extraction and automatic segmentation of brain images. NeuroImage 2002;17(3):1087–100.

Lee JM, Yoon U, Nam SH, Kim JH, Kim IY, Kim SI. Evaluation of automated and semi-automated skull-stripping algorithms using similarity index and segmentation error. Computers in Biology and Medicine 2003;33(6):495–507.

Lemieux L, Hagemann G, Krakow K, Woermann FG. Fast, accurate, and reproducible automatic segmentation of the brain in T1-weighted volume MRI data. Magnetic Resonance in Medicine 1999;42(1):127–35.

Lemieux L, Hammers A, Mackinnon T, Liu RS. Automatic segmentation of the brain and intracranial cerebrospinal fluid in T1-weighted volume MRI scans of the head, and its application to serial cerebral and intracranial volumetry. Magnetic Resonance in Medicine 2003;49(5):872–84.

Leung KK, Barnes J, Modat M, Ridgway GR, Bartlett JW, Fox NC, Ourselin S. Brain MAPS: An automated, accurate and robust brain extraction technique using a template library. NeuroImage 2011;55(3):1091–108.

Liu JX, Chen YS, Chen LF. Accurate and robust extraction of brain regions using a deformable model based on radial basis functions. J of Neuroscience Methods 2009;182(2):255–66.

Lorensen WE, Cline HE. Marching cubes: A high-resolution 3D surface construction algorithm. SIGGRAPH Comput Graph 1987;21(4):163–9.

MacDonald D, Kabani N, Avis D, Evans AC. Automated 3-D extraction of inner and outer surfaces of cerebral cortex from MRI. NeuroImage 2000;12(3):340–56.

Matula P. Effectivity of spherical object reconstruction using star-shaped simplex meshes. In: First International Symposium on 3D Data Processing Visualization and Transmission. 2002. p. 794–9.

Meijering E. A chronology of interpolation: From ancient astronomy to modern signal and image processing. In: Proceedings of the IEEE. 2002. p. 319–42.

Merisaari H, Parkkola R, Alhoniemia E, Teräs M, Lehtonend L, Haataja L, Lapinleimu H, Nevalainen OS. Gaussian mixture model-based segmentation of MR images taken from premature infant brains. J of Neuroscience Methods 2009;182(1):110–22.

Mikheev A, Nevsky G, Govindan S, Grossman R, Rusinek H. Fully automatic segmentation of the brain from T1-weighted MRI using bridge burner algorithm. J of Magnetic Resonance Imaging 2008;27(6):1235–41.

Moré JJ. The Levenberg-Marquardt algorithm: Implementation and theory. In: Watson GA, editor. Numerical Analysis. Berlin: Springer; 1977. p. 105–16.

Otsu N. A threshold selection method from gray-level histograms. IEEE Trans on Systems, Man and Cybernetics 1979;9(1):62–6.

Park H, Seo J, the ADNI . Application of multidimensional scaling to quantify shape in alzheimer's disease and its correlation with mini mental state examination: A feasibility study. J of Neuroscience Methods 2011;194(2):380–5.

Park JG, Lee C. Skull stripping based on region growing for magnetic resonance brain images. NeuroImage 2009;47(4):1394–407.

Perez CA, Gonzalez GD, Medina LE, Galdames FJ. Linear versus nonlinear neural modeling for 2-D pattern recognition. IEEE Trans on Systems Man and Cybernetics Part A-Systems and Humans 2005;35(6):955–64.

Perona P, Malik J. Scale-space and edge detection using anisotropic diffusion. IEEE Trans on Pattern Analysis and Machine Intelligence 1990;12:629–39.

PLOMO . Website of the STIC-AmSud "PLOMO" project. http://liris.cnrs.fr/plomo.

Rehm K, Schaper K, Anderson J, Woods R, Stoltzner S, Rottenberg D. Putting our heads together: a consensus approach to brain/non-brain segmentation in T1-weighted MR volumes. NeuroImage 2004;22(3):1262–70.

Rex DE, Ma JQ, Toga AW. The LONI pipeline processing environment. NeuroImage 2003;19(3):1033–48.

Rex DE, Shattuck DW, Woods RP, Narr KL, Luders E, Rehm K, Stolzner SE, Rottenberg DA, Toga AW. A meta-algorithm for brain extraction in MRI. NeuroImage 2004;23(2):625–37.

Richard A. Biomedical Imaging, Visualization, and Analysis. New York, NY, USA: John Wiley & Sons, Inc., 2000.

Rosenblatt M. Remarks on some nonparametric estimates of a density function. Annals of Mathematical Statistics 1956;27(3):832–7.

Sadananthan SA, Zheng W, Chee MWL, Zagorodnov V. Skull stripping using graph cuts. Neuroimage 2010;49(1):225–39.

Sandor S, Leahy R. Surface-based labeling of cortical anatomy using a deformable atlas. IEEE Trans on Medical Imaging 1997;16(1):41–54.

Ségonne F, Dale AM, Busa BE, Glessner BM, Salat BD, Hahn BHK, A BF. A hybrid approach to the skull stripping problem in MRI. NeuroImage 2004;22:1060–75.

Shan Z, GH Y, Liu J. Automated histogram-based brain segmentation in T1-weighted three-dimensional magnetic resonance head images. Neuroimage 2002;17(3):1587–98.

Shattuck DW, Prasad G, Mirza M, Narr KL, Toga AW. Online resource for validation of brain segmentation methods. NeuroImage 2009;45(2):431–9.

Shattuck DW, Sandor-Leahy SR, Schaper KA, Rottenberg DA, Leahy RM. Magnetic resonance image tissue classification using a partial volume model. NeuroImage 2001;13:856–76.

Smith S. Fast robust automated brain extraction. Human Brain Mapping 2002;17(3):143–55.

Somasundaram K, Kalaiselvi T. Automatic brain extraction methods for T1 magnetic resonance images using region labeling and morphological operations. Computers in Biology and Medicine 2011;41(8):716–25.

Tejos C, Irarrazaval P. Simplex mesh diffusion snakes: Integrating 2D and 3D deformable models and statistical shape knowledge in a variational framework. Int J Comput Vision 2009;85(1):19–34.

Thompson PM, Mega MS, Woods RP, Zoumalan CI, Lindshield CJ, Blanton RE, Moussai J, Holmes CJ, Cummings JL, Toga AW. Cortical change in alzheimer's disease detected with a disease-specific population-based brain atlas. Cerebral Cortex 2001;11(1):1–16.

Tosun D, Rettmann ME, Naiman DQ, Resnick SM, Kraut MA, Prince JL. Cortical reconstruction using implicit surface evolution: Accuracy and precision analysis. NeuroImage 2006;29(3):838–52.

Wang L, Chen Y, Pan X, Hong X, Xia D. Level set segmentation of brain magnetic resonance images based on local gaussian distribution fitting energy. J of Neuroscience Methods 2010;188(2):316–25.

Ward BD. 3dIntracranial: Automatic segmentation of intracranial region. 1999. afni.nimh.nih.gov/afni/doc/manual/3dIntracranial/.

Weese J, Kaus MR, Lorenz C, Lobregt S, Truyen R, Pekar V. Shape constrained deformable models for 3-D medical image segmentation. Image Processing in Med Imag (IPMI), Lecture Notes Computer Science 2001;2082:380–7.

Wels M, Zheng Y, Huber M, Hornegger J, Comaniciu D. A discriminative model-constrained EM approach to 3D MRI brain tissue classification and intensity non-uniformity correction. Phys Med Biol 2011;56(11):3269–300.

Yoon UC, Kim JS, Kim JS, Kim IY, Kim SI. Adaptable fuzzy C-means for improved classification as a preprocessing procedure of brain parcellation. J Digit Imaging 2001;14(2):238–40.

Zhao L, Ruotsalainen U, Hirvonen J, Hietala J, Tohka J. Automatic cerebral and cerebellar hemisphere segmentation in 3D MRI: Adaptive disconnection algorithm. Medical Image Analysis 2010;14(3):360–72.

Zhuang AH, Valentino DJ, Toga AW. Skull-stripping magnetic resonance brain images using a model-based level set. NeuroImage 2006;31(1):79–92.

Zorin D, Schröder P, Sweldens W. Interpolating subdivisions for meshes with arbitrary topology. In: Proceedings of the 23rd annual conference on Computer graphics and interactive techniques. New York, NY, USA: ACM; SIGGRAPH '96; 1996. p. 189–92.